

Hyperspectral and Multispectral Classification for Coastal Wetland Using Depthwise Feature Interaction Network

Yunhao Gao, Wei Li, Mengmeng Zhang, Jianbu Wang, Weiwei Sun, Ran Tao, Qian Du

Abstract—The monitoring of coastal wetlands is of great importance to the protection of marine and terrestrial ecosystems. However, due to the complex environment, severe vegetation mixture, and difficulty of access, it is impossible to accurately classify coastal wetlands and identify their species with traditional classifiers. Despite the integration of multisource remote sensing data for performance enhancement, there are still challenges with acquiring and exploiting the complementary merits from multisource data. In this paper, the Depthwise Feature Interaction Network (DFINet) is proposed for wetland classification. A depthwise cross attention module is designed to extract self-correlation and cross-correlation from multisource feature pairs. In this way, meaningful complementary information is emphasized for classification. DFINet is optimized by coordinating consistency loss, discrimination loss, and classification loss. Accordingly, DFINet reaches the standard solution-space under the regularity of loss functions, while the spatial consistency and feature discrimination are preserved. Comprehensive experimental results on two hyperspectral and multispectral wetland datasets demonstrate that the proposed DFINet outperforms other competitive methods in terms of overall accuracy.

Index Terms—Convolutional neural network, wetland classification, hyperspectral and multispectral, depthwise feature interaction network (DFINet).

I. INTRODUCTION

Wetland is one of the three important natural ecosystems on the Earth, and plays an important role in the global carbon cycle. It is of great significance for purifying pollution, conserving water source and regulating climate [1]. However, wetlands have shown a trend of degradation or even disappearance in the world due to inappropriate anthropogenic activities. Therefore, it is urgent to protect wetlands wherein monitoring land-cover is essential [2]. Wetland monitoring has attracted considerable attention [3] [4]. Nevertheless, manual investigation is difficult, because of the special conditions of wetlands. It brings about great challenges to wetland monitoring.

This paper is supported by the Beijing Natural Science Foundation (Grant nos. JQ20021), National Natural Science Foundation of China (Grant nos. 61922013, 61421001 and U1833203). (Corresponding author: Wei Li)

Y. Gao, W. Li, M. Zhang, and R. Tao are with the School of Information and Electronics, Beijing Institute of Technology, Beijing 100081, China (e-mail: liwei089@ieee.org).

J. Wang is with the Lab of Marine Physics and Remote Sensing, First Institute of Oceanography, Ministry of Natural Resources Qingdao, China (email: wangjianbu@fio.org.cn).

W. Sun is with the Department of Geography and Spatial Information Techniques, Ningbo University, Ningbo 315211, China (e-mail: sunweiwei@nbu.edu.cn).

Q. Du is with the Department of Electrical and Computer Engineering, Mississippi State University, Starkville, MS 39762 USA (e-mail: du@ece.msstate.edu).

Earth observation systems have been developed rapidly in recent years, thus supply a large number of observation data for wetland [5]. Available data for surface analysis include hyperspectral image (HSI), light detection and ranging (LiDAR) data, multispectral image (MSI), optical image, etc. Especially, high spatial and spectral resolution data provide plenty of information for wetland [6]. Accordingly, finer classification for wetlands based on remote sensing data has become an active research field. There are extensive wetland objects with complex spatial structure and serious phenomenon of “inconsistency between spectrum and objects”. Wetland classification is still a challenging task.

Recently, many classification frameworks have been successfully applied to coastal wetland. Machine learning deserves special attention, because of the relevant performance over wetland classification. In [7], the classification results of deep convolutional neural network (CNN) were compared with those of random forest to evaluate the efficiency of CNN. In [8], the Fisher linear discriminant analysis (FLDA) and physical interpretation were employed on polarimetric synthetic aperture radar (SAR) data to obtain the coefficient of coherency matrix. Delancey *et al.* [9] investigated the performance of deep CNN on large-scale wetland classification. In [10], 3D-CNN was utilized for feature extraction and classification of wetland MSI. In [11], low-rank representation with elastic net was proposed for coastal wetland classification by using GaoFen-5 (GF-5) HSI of China. Liu *et al.* [12] employed inter-class sparsity based discriminative least square regression on coastal wetland data, which encourages intra-class differences and inter-class similarities. Besides, Some of the most noteworthy approaches also achieved breakthrough by using random forest (RF), support vector machine (SVM), and multiobject CNN [13] [14] [15].

Although the above classification models have shown great success in wetland classification, they still misjudge similar wetland surfaces, especially vegetation. Due to complementary information provided by multisource data, they are helpful for comprehensive feature representation. Therefore, multisource data are beneficial to complex classification tasks with complementary information. A variety of works have been done towards the integration of multisource information for classification.

To make full use of the complementary information, the fusion strategy is taken into accounts, such as data fusion, feature fusion, and decision fusion. Data fusion is a fundamental fusion strategy, such as directly stacking and fusion

based on topological structure [16]. Then feature extraction and classification are executed [17]. In [18], the Gram-Schmidt algorithm was utilized to fusing the optical image and SAR image, and then the optimal segmentation hyperplane was constructed by SVM. In [19], complementary information was utilized for multisource data fusion by calculating the adaptive locality weight. However, data redundancy or data loss is inevitable in data fusion.

For feature fusion, Chen *et al.* [20] employed deep CNN to extract heterogeneous features which are fused by fully-connected layer. Later, Xu *et al.* [21] proposed a two-branch CNN for HSI and LiDAR data classification. A two-tunnel CNN framework with cascade block was contrapuntally developed to extract features from HSI and LiDAR data. In [22], an unsupervised multiscale framework was designed for feature extraction from multisource data. Then, the fused features are fed into fully-connected layers. In [23], extinction profiles (EPs) was utilized for feature extraction first. The extracted features are then fused by deep CNN. In [24], multisensor composite kernels (MCK) scheme was proposed to fuse the features extracted by a three-stream CNN. In [25], a hierarchical random walk network (HRWN) was designed to preserve boundary localization and spatial consistency of multisource data. In addition, graph-based feature fusion also achieves good results [26] [27].

Decision fusion usually requires multiple classifiers to produce an optimal result. In [28], an ensemble multiple kernel active learning framework was designed to incorporate different types of features, and then decision fusion was implemented to achieve the final decision based on the probabilistic outputs. Zhong *et al.* [29] proposed an optimal decision fusion for urban land-use/land-cover classification based on adaptive differential evolution. In [30], a coupled CNN was designed for feature extraction, and the classification map was achieved by weighted summation. Liao *et al.* [31] proposed a multisource data classification method by combining feature and decision fusion. Extracted and fused features are individually fed into a SVM classifier, and then four classification maps are fused by the weighted majority voting. Both feature fusion and decision fusion have achieved promising results on multisource data.

Generally speaking, most of the above methods are based on HSI, and other data sources assist in classification. Although HSI is rich in spectral information that is conducive to wetland classification, it is often accompanied by inconsistency between spectrum and objects [32] [33] [34]. Moreover, the spatial resolution of HSI is generally lower than that of other data sources. On the contrary, MSI provides high-resolution spatial information. Therefore, HSI from GF-5 is used for wetland classification with the assistance of MSI from Sentinel-2. CNN-based feature extraction significantly boosts the performance. However, the imbalance of feature representation and the Hughes phenomenon still hinder the research of wetland classification. To better utilize multisource information, the following two problems need to be addressed: 1) how to preserve the feature discrimination between different classes while eliminating the modal differences, and 2) how to make full use of the complementary information of HSI and MSI.

Thus, a novel wetland classification model on HSI and MSI named Deepwise Feature Interaction Network (DFINet) is proposed. Firstly, two branches of CNN with different parameters are used to extract features from HSI and MSI. To preserve the feature discrimination of different semantics and eliminate the discrepancy of multisource data as well, we minimize the loss of measurement in the label space to encourage the discrimination of CNN features. Meanwhile, we minimize the distance measurement in the common feature space to enhance the spatial consistency. To make full use of the complementary information, a depthwise cross attention module (DCAM) is adopted for the semantic correlation between heterogeneous features, so that meaningful features are emphasized.

The main contributions of this paper are summarized as follows.

- An end-to-end joint classification framework named DFINet is designed to bridge the multisource wetland data. The complementary merits of HSI and MSI are brought into full play. Furthermore, because of the regularization of feature space and label space, DFINet still performs well with few training samples.
- A DCAM is well-designed to make full use of the complementary information. Self-correlation and cross-correlation enhance the interaction of HSI and MSI. Different from the traditional attention mechanism, DCAM generates a kernel to draw cross attention from one data source to another one. Therefore, the strong self-correlation is emphasized, and the weak one is suppressed.
- To preserve discrimination, while eliminating the differences, two loss functions are applied to common feature space and label space. Specifically, the distance loss is minimized in the common feature space to ensure the consistency of HSI and MSI. The discrimination loss is minimized to preserve feature discrimination. Finally, an additional cross-entropy loss is employed to achieve the sample discrimination after the feature projection. Thus, the solution is regularized into a smaller range, which promotes the performance of classification.

The rest of this paper is organized as follows. In Section II, the proposed model is described in detail. Section III provides the description of datasets and experimental results. Finally, Section IV concludes this paper.

II. PROPOSED CLASSIFICATION FRAMEWORK

This section describes the proposed DFINet that automatically extracts features and fuse them effectively. As shown in Fig. 1, it includes a feature extraction network and a DCAM, followed by a fully-connected (FC) layer¹.

In this paper, HSI is the main data source with a corresponding ground truth map, and MSI is the auxiliary data source. Even though the main purpose of this work is joint classification using HSI and MSI. Registration is necessary preprocessing for multisource remote sensing data. Considering the correspondence between the ground truth map and HSI,

¹The codes of DFINet are available at: https://github.com/formango/HSI_MSI_Classification

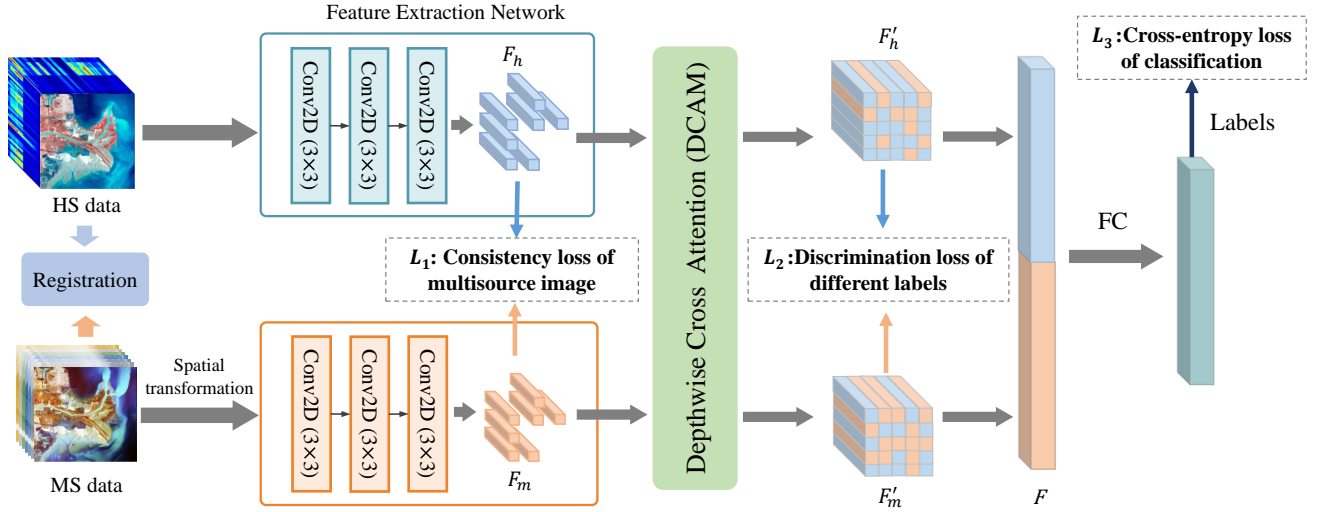


Fig. 1. Schematic illustration of the proposed depthwise feature interaction network (DFINet). Firstly, HSI and MSI are registered, and the spatial resolution remains unchanged. Then, spatial transformation is employed to achieve the unification of size without information loss. After that, the patches of HSI and MSI on coastal wetland are fed into feature extractors, respectively. The interaction between HSI and MSI is achieved by depthwise cross attention module, thus the inter-modal complementary information is fully extracted. Finally, three loss terms are utilized to assist the optimization. Therefore, the consistency of feature space and feature discrimination are preserved.

the experimental data are registered with HSI as reference, and MSI is the sensed image. The algorithm in [35] is utilized for image registration². The registration algorithm is performed on band images from HSI and MSI which are randomly selected. After registration, both HSI and MSI keep their spatial resolution. The reference image is first upsampled to the same size as the sensed image. Next a Harris corner detector is performed to generate the keypoints of the reference image and the sensed image. Meanwhile, an image pyramid is constructed based on the Scale-Space Theory, and then the multiscale PIIFD descriptor is employed on Harris corners in image pyramid [36]. Thus, the influence of scale difference between HSI and MSI is alleviated. Finally, the best-bin-first (BBF) algorithm is utilized for keypoints matching [37]. The outlier elimination is realized by keeping the consistency of main direction and spatial distribution. Then, parameters of the similarity transformation model are estimated by the least squares method, and used for the registration of entire HSI and MSI.

A. Feature Extraction Network

CNN has been proved to be capable of feature extraction. Therefore, two feature extraction networks with different parameters are utilized to extract spatial-spectral information from HSI and MSI. Given a HSI $X_{HSI} \in \mathbb{R}^{c_1 \times h \times w}$ and a registered MSI $X_{MSI} \in \mathbb{R}^{c_2 \times 3h \times 3w}$. Considering the resolution inconsistency between HSI and MSI, the spatial size of the registered multisource data is unified through spatial transformation as shown in Fig. 2. The 2D spatial information in a band of MSI is grouped into as channel, and then stacked to form a 3D cube. Finally, the same

operation is performed on each band to obtain the transformed MSI ($X_{MSI}^T \in \mathbb{R}^{9c_2 \times h \times w}$). To our knowledge, the spatial transformation is a linear transformation, information loss is avoided compared with the traditional downsampling methods. Besides, compared with convoluting X_{MSI} directly, the receptive field of convolution kernel is enlarged while the parameters are reduced, due to the smaller spatial size of X_{MSI}^T [38].

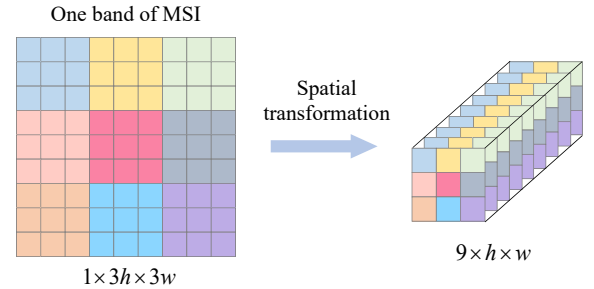


Fig. 2. Illustration of the spatial transformation.

To independently extract the spatial-spectral features, spatial patches centered at the position p_{ij} ($0 < i < h, 0 < j < w$) with patch size r are fed into the feature extractor. The feature extractor is a 2D-CNN with three convolution layers.

For HSI, the feature extraction network is designed as $\text{ConvBN}(c_1, 256) \rightarrow \text{ConvBN}(256, 128) \rightarrow \text{ConvBN}(128, 128)$. For MSI, features are extracted by $\text{ConvBN}(9c_2, 128) \rightarrow \text{ConvBN}(128, 128) \rightarrow \text{ConvBN}(128, 128)$. $\text{ConvBN}(c, c')$ is a convolution layer sequentially followed by a batch normalization (BN) layer and an activation layer, and c and c' mean the number of input channels and output channels, respectively. The extracted features F_h and F_m are further interacted by a DCAM.

²The codes of registration are available at: <https://github.com/MrPingQi/MS-PIIFD-registration>

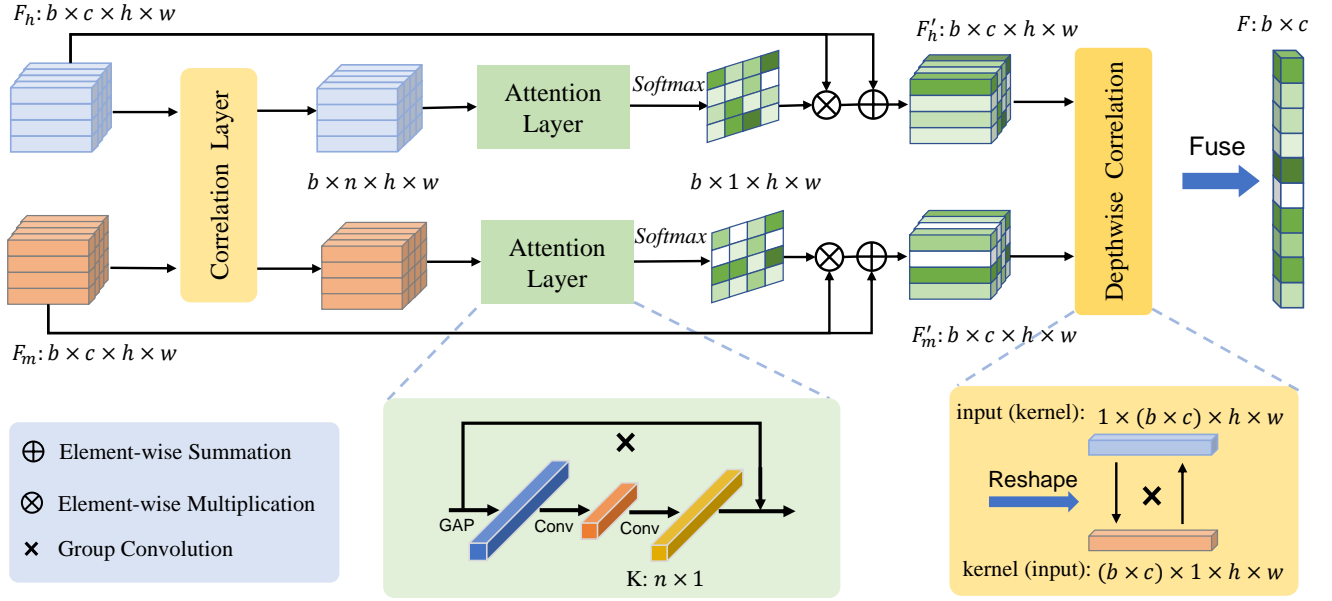


Fig. 3. Illustration of the depthwise cross attention module (DCAM).

B. Depthwise Cross Attention Module

Multisource fusion based on aggregation has made great breakthrough in computer vision [39]. Several sub-networks are aggregated into an end-to-end framework by summation, averaging, concatenation, or attention mechanism [40] [41]. However, aggregation-based methods tend to ignore the information interaction between multisource data. In [42], a spatial-spectral attention module was designed to extract the meaningful information and the correlation of adjacent pixels, which achieves effective performance in interpretation of HSI. Recently, a variety of works have been done towards feature interaction, such as cross attention network [43] [44]. However, these methods focus on constructing the attention map of single data source, but ignore the correlation of multisource data. Therefore, to make full use of the complementary information, the DCAM is designed to enhance the correlation between heterogeneous features. Firstly, the attention map is generated by the correlation of multisource features in corresponding positions, which emphasizes the information with strong correlation and suppresses the weak one. Then, the depthwise correlation is designed to explore the cross-correlation between features. In this way, the multisource features are deeply integrated rather than concatenation or averaging. Therefore, features are weighted with cross attention maps to achieve self-correlation, and then cross-correlation is further reached by depthwise interaction.

The flowchart of DCAM is illustrated in Fig. 3. The above feature maps from HSI and MSI ($F_h \in \mathbb{R}^{c \times w \times h}$ and $F_m \in \mathbb{R}^{c \times w \times h}$). Here w and h denote the width and height, respectively, and c is the number of channels. Firstly, the correlation layer is designed to calculate the correlation map between F_h and F_m . F_h and F_m are firstly reshaped to $\mathbb{R}^{c \times n}$, $n = h \times w$. In this way, $F_h = [h_1, h_2, \dots, h_n]$ and $F_m = [m_1, m_2, \dots, m_n]$. Therefore, the semantic relevance between h_i and m_j is computed by cosine distance:

$$C_{ij} = \left(\frac{h_i}{\|h_i\|_2} \right)^T \left(\frac{m_j}{\|m_j\|_2} \right) \quad i, j = 1, 2, \dots, n \quad (1)$$

Here $\|\cdot\|_2$ denotes the L_2 -Norm, and the correlation maps $C_h \in \mathbb{R}^{n \times h \times w}$ and $C_m \in \mathbb{R}^{n \times h \times w}$ between HSI and MSI are produced.

Furthermore, the correlation maps guide the generation of cross attention maps. Taking C_m for example, the attention layer is illustrated in green rectangle of Fig. 3, where the correlation map C_m are firstly squeezed in the spatial domain by global average pooling (GAP). The global feature descriptors $C_g \in \mathbb{R}^{n \times 1}$ are generated. The feature descriptors are then fed into two 2D-Conv layers to generate the kernel. The kernel K is denoted as:

$$K = W_2 \cdot \sigma_r(W_1 C_g) \quad (2)$$

where $W_1 \in \mathbb{R}^{\frac{n}{\gamma} \times n}$ and $W_2 \in \mathbb{R}^{n \times \frac{n}{\gamma}}$ denote the weights of the 2D-Conv layers with kernel size 1×1 , and γ is reduction ratio. Here, 2D-Conv is utilized to adaptively adjust the weight of channels in correlation map. $\gamma = 9$ is utilized to reduce the parameters. If only one 2D-Conv layer is used, the number of parameters is n^2 . When γ is introduced, the number of parameters from two 2D-Conv layers is $\frac{2n^2}{\gamma}$. Obviously, the number of parameters is reduced by $2/\gamma$. σ_r is the *ReLU* function. $K \in \mathbb{R}^{n \times 1}$ is the kernel that draws cross attention to HSI. The non-mutually-exclusive relationship is obtained by $V = \sigma_{so}(K^T C_m)$, σ_{so} is the *Softmax* function. Here a larger $V \in \mathbb{R}^{h \times w}$ represents more meaningful features. Thus, the final discriminative feature maps F'_m are computed by residual attention mechanism:

$$F'_m = F_m \cdot V + F_m \quad (3)$$

Similarly, F'_h is obtained. Therefore, the self-correlations of multisource feature pairs are achieved.

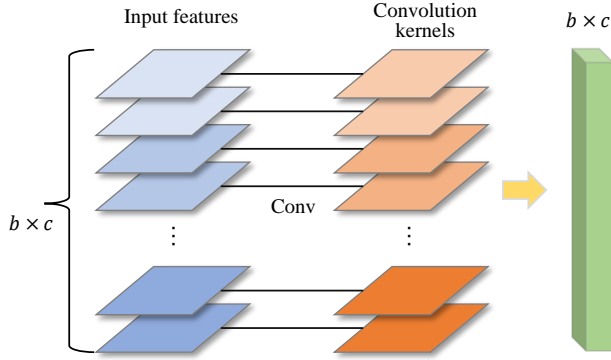


Fig. 4. Illustration of the depthwise correlation.

Multisource data classification based on feature fusion usually executes feature integration by concatenation or averaging. However, the relationship of parameters from different data sources is weakened, and the number of parameters in the full-connected layer is significantly increased. To address these problems, the depthwise correlation layer is adopted to excavate the cross-correlation of multisource feature pairs. In this paper, the cross-correlation F_{h-m} from $F'_h \in \mathbb{R}^{b \times c \times h \times w}$ to $F'_m \in \mathbb{R}^{b \times c \times h \times w}$ is computed by a group convolution operator. To achieve the depth interaction from F'_h to F'_m , a set of convolution kernels are defined according to F'_m . Then, the defined convolution kernels are utilized to convolute F'_h for feature integration. As shown in Fig. 4, cross-correlation is calculated using features in a batch. Thus, the integrated feature F is generated.

More specifically, F'_m is firstly reshaped to $[b \times c, 1, h, w]$ as the convolution kernels. Here, $b \times c$ is the number of convolution kernels, and $h \times w$ is kernel size. Next, F'_h is reshaped to $[1, b \times c, h, w]$ as the input features, where $b \times c$ denotes the number of features, $h \times w$ is the size of input features. Then F_{h-m} is calculated as:

$$F_{h-m} = F'_h * F'_m \quad (4)$$

where $*$ denotes the group convolutional operator, and the number of groups is $b \times c$. Similarly, F_{m-h} denotes the cross-correlation from $F'_m \in \mathbb{R}^{b \times c \times h \times w}$ to $F'_h \in \mathbb{R}^{b \times c \times h \times w}$. After reshaping F'_m to $[b \times c, 1, h, w]$ as the convolution kernels and reshaping F'_h to $[1, b \times c, h, w]$ as the input features, F_{m-h} is calculated by $F_{m-h} = F'_m * F'_h$. Thus, multisource features $F = F_{h-m} = F_{m-h}$ are integrated through parameter optimization.

The DCAM encourages the interaction of multisource features. Through the attention mechanism, the strong self-correlation is emphasized, and the weak one is suppressed. The depthwise correlation layer further enhances the correlation to integrate the multisource features.

C. Objective Function

The proposed classification model is optimized in an end-to-end manner by the training set $X_{train} = (x^h, x^m, y)$. Here, y is the real label of HSI and MSI patch (x^h, x^m) . The fully-connected layers and *softmax* are employed at the end of

the network. In this way, the prediction vectors are achieved through feature representation. Therefore, the classification loss is defined as:

$$L_3 = \frac{1}{N} \sum_{i=1}^N \sum_{c=1}^C -y_i^c \log p_i^c, \quad (5)$$

where L_3 is the cross-entropy loss between the real labels and the output of DFNet. N is batch size, and y is the label, if the class is c , then $y^c = 1$, otherwise 0. p^c is the prediction probability after *softmax*.

Furthermore, the discrimination loss in the label space is designed to encourage the discrimination between different classes. We first calculate the cosine similarity of two vectors, and the probability value of similarity is obtained by *Sigmoid* function. In the training stage, the probability value of two vectors of the same class should be maximized, and vice versa. Therefore, feature discrimination of different labels is enhanced. The discrimination loss is computed by:

$$L_2 = \underbrace{\frac{1}{N^2} \sum_{i,j=1}^N (\log(1 + e^{\theta_{ij}^{hm}}) - \delta_{ij} \theta_{ij}^{hm})}_{\text{HSI and MSI modality}} + \underbrace{\frac{1}{N^2} \sum_{i,j=1}^N (\log(1 + e^{\theta_{ij}^{mm}}) - \delta_{ij} \theta_{ij}^{mm})}_{\text{MSI modality}} + \underbrace{\frac{1}{N^2} \sum_{i,j=1}^N (\log(1 + e^{\theta_{ij}^{hh}}) - \delta_{ij} \theta_{ij}^{hh})}_{\text{HSI modality}}, \quad (6)$$

Here, $\theta_{ij} = \frac{1}{2} \cos(v_i, u_j)$ denotes the cosine similarity. v_i, u_j are the features from the depthwise correlation layer, and $\delta_{ij} = 1(v_i, u_j)$ is the logistic function, whose value is 1 if the two features are the representation of same classes, otherwise 0. Obviously, L_2 indicates the negative log-likelihood of θ_{ij} . The likelihood function is denoted as:

$$p(\delta_{ij}|u_i, v_j) = \begin{cases} \sigma_{si}(\theta_{ij}), & \delta_{ij} = 1, \\ 1 - \sigma_{si}(\theta_{ij}), & \text{otherwise}, \end{cases} \quad (7)$$

where $\sigma_{si}(\cdot)$ is *Sigmoid* function. When the negative log-likelihood function is minimized, the likelihood is maximized. Likelihood is the probability value from σ_{si} . Therefore, when the similarity of inter-modal samples θ_{ij} is larger, the $p(1|u_i, v_j)$ is larger. That is to say, samples of the same class have higher likelihood, while samples of different classes have lower likelihood. Therefore, the feature discrimination is enhanced.

Spatial consistency captures common patterns in multisource data, which is the foundation of feature interaction [45] [46]. In this paper, we minimize the distance between samples in the feature space. The consistency loss is formulated as:

$$L_1 = \frac{1}{N} \|F_1 - F_2\|_2, \quad (8)$$

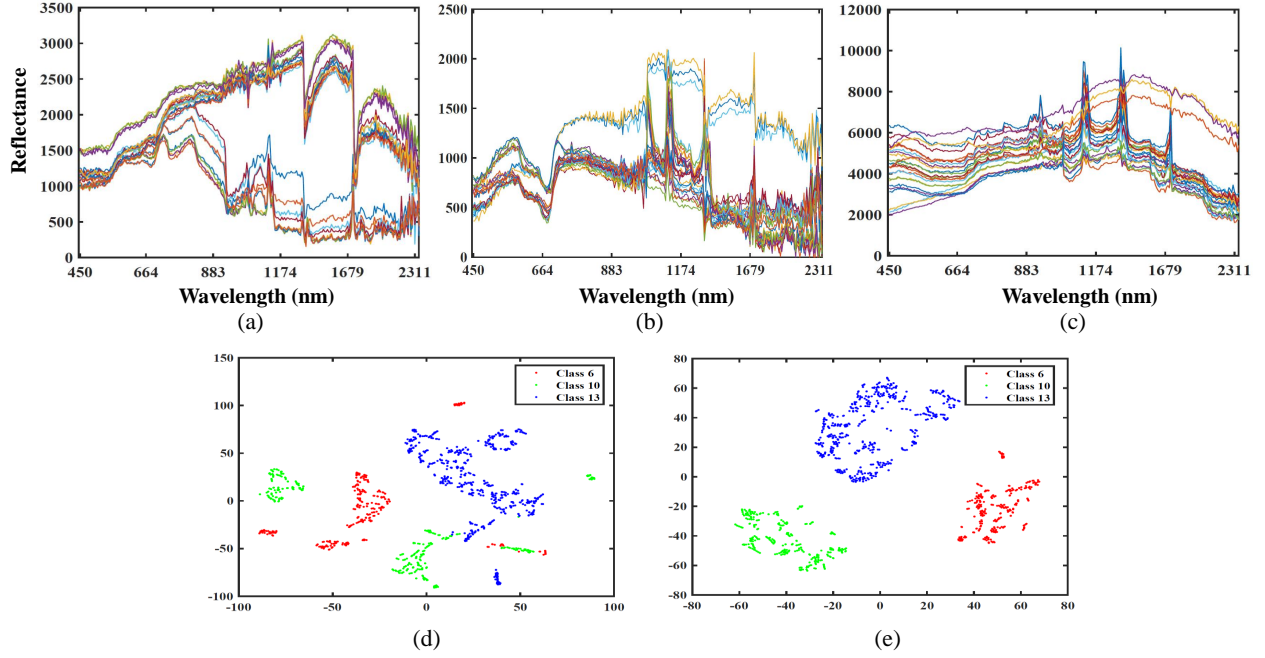


Fig. 5. The spectral pattern and data distribution of Yancheng GF-5 data. (a) The spectral pattern of class-6. (b) The spectral pattern of class-10. (c) The spectral pattern of class-13. (d) The data distribution of class-6, class-10, and class-13 in Yancheng GF-5 data. (e) The data distribution of the outputs from the proposed DFNet in Yancheng GF-5 data.

where F_1 and F_2 are the features from the feature extraction network, and $\|\cdot\|_2$ denotes the L_2 -Norm.

The final loss function is achieved by combining L_1 , L_2 , and L_3 :

$$L = \lambda_1 L_1 + \lambda_2 L_2 + L_3, \quad (9)$$

where λ_1 and λ_2 are the hyperparameters to control the contributions. Stochastic gradient descent (SGD) is employed to optimize the whole model. The entire network is trained on an Nvidia GTX 1060 GPU in PyTorch.

D. Analysis on the Proposed Method

Considering the heterogeneity and complementarity of multisource wetland data, a classification method based on CNN is designed. To make full use of the complementary merits of HSI and MSI, DCAM is applied to obtain the self-correlation and cross-correlation of multisource feature pairs, as deep interaction promotes feature fusion. Fig. 5 exhibits spectral pattern and data distribution of some typical classes in GF-5 Yancheng data. From Fig. 5 (a)-(c), we find the inconsistency in spectral and object information, which deteriorates the performance as shown in Fig. 5 (d).

In fact, it is difficult to eliminate spectral differences by feature decomposition and transformation. In this paper, the discrimination loss is utilized to standardize the feature discrimination of different classes. Therefore, inter-class dissimilarity is enlarged and intra-class variation is alleviated. In addition, consistency loss is optimized to obtain the common patterns of HSI and MSI. In Fig. 5 (e), pixels of the same classes are closer to each other, while a large margin separates pixels in different classes, which indicates that the proposed DFNet achieves good performance.

Compared with several classification methods in Section III, the feature interaction of DFNet is more thorough, and the joint optimization of multiple loss functions promotes the excellent performance in coastal wetland, including the few-shot scene.

III. EXPERIMENTAL RESULTS AND ANALYSIS

A. The Description of Dataset

To fully utilize the advantages of multisource remote sensing data, GaoFen-5 (GF-5) and Sentinel-2 data are utilized for analysis. The spatial resolution of GF-5 is 30m, and 10m spatial resolution is selected in Sentinel-2. The spectral resolution of GF-5 is 5nm in VNIR (400nm-1000nm) and 10nm in SWIR (1000nm-2500nm), in which the number of bands is 150 and 180, respectively. The spectral resolution of Sentinel-2 is 15nm-180nm. In order to maintain time consistency and avoid the deterioration of pixel misalignment, this paper uses data graphics with similar time to analyze. Moreover, it is necessary to perform data preprocessing steps (including spatial registration, geometric correction, atmospheric correction, image clipping, and merging) for HSI and MSI [47]. To be specific, the Fast Line-of-Sight Atmospheric Analysis of Spectral Hypercubes (FLAASH) module of ENVI is utilized to carry out atmospheric correction on all datasets of GF-5. Radiometric calibration of GF-5 data is achieved by gain and offset coefficients. Atmospheric correction and radiometric calibration of Sentinel-2 datasets are implemented on the sentinel application platform (SNAP).

The first experimental dataset is Yancheng Wetland scene. As shown in Fig. 6 (a) and (b), the hyperspectral and multispectral data of Yancheng were captured on April 4,

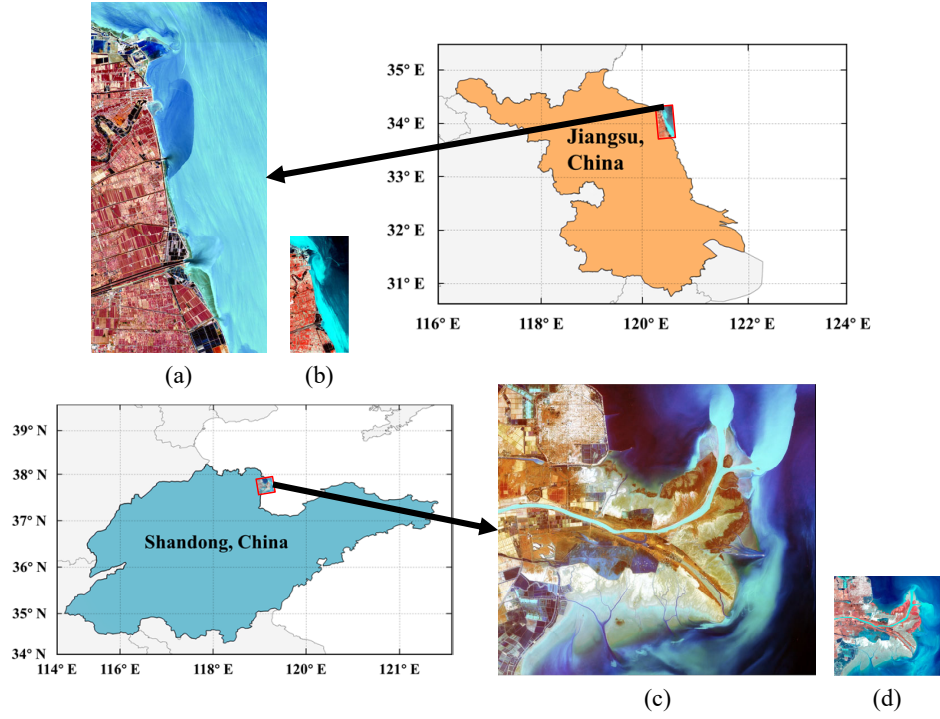


Fig. 6. The wetland datasets. (a) Image captured by Sentinel-MSI in Yancheng. (b) Image captured by GF5-HSI in Yancheng. (c) Image captured by Sentinel-MSI in Yellow River Estuary. (d) Image captured by GF5-HSI in Yellow River Estuary.

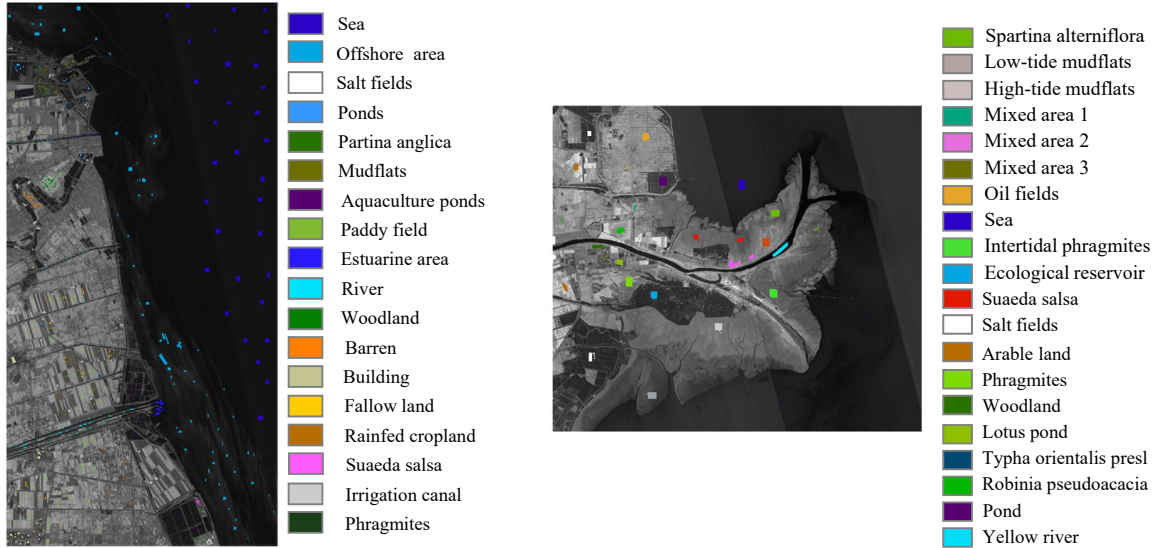


Fig. 7. The region of interest and ground truth maps for two experimental wetland datasets.

2019 and March 29, 2019. The size of Yancheng dataset is 1175×585 pixels of HSI (the bad bands are 1-14, 88, and 129-133 in VNIR and 42-51, 96-115, 119-123, 171-173, and 175-180 in SWIR) and 3525×1755 pixels of MSI. Yancheng Wetland has a coastline of 582 km, which is located in the east of Jiangsu Province in China ($32^{\circ}34' - 34^{\circ}28'N$, $119^{\circ}27' - 121^{\circ}16'E$). Yancheng is rich in wetland resources, with a large area of radiating sandbars, coastal forest farms and grasslands. The real label of the region of interest (ROI)

is obtained by integrating prior knowledge and photo interpretation from high spatial resolution images as shown in Fig. 7. Then training and testing samples are randomly selected from ROI as listed in Table I, in which the geographical proximity and spacing are fully considered without overlapping regions. Then training and testing samples are randomly selected from ROI as listed in Table I, in which the geographical proximity and spacing are fully considered without overlapping regions.

The second dataset is Yellow River Estuary scene. As shown

TABLE I
NUMBER OF TRAINING AND TESTING SAMPLES FOR WETLAND DATASETS.

| Yancheng dataset | | | | Yellow River Estuary dataset | | | |
|------------------|------------------|-------------------|---------|------------------------------|------------------------|-------------------|---------|
| Class | | Number of Samples | | Class | | Number of Samples | |
| No. | Name | Training | Testing | No. | Name | Training | Testing |
| 1 | Sea | 209 | 2186 | 1 | Spartina alterniflora | 84 | 743 |
| 2 | Offshore area | 140 | 1448 | 2 | Low-tide mudflat | 84 | 709 |
| 3 | Salt field | 6 | 104 | 3 | High-tide mudflat | 91 | 645 |
| 4 | Pond | 20 | 173 | 4 | Mixed area 1 | 16 | 123 |
| 5 | Partina anglica | 7 | 76 | 5 | Mixed area 2 | 95 | 774 |
| 6 | Mudflats | 25 | 243 | 6 | Mixed area 3 | 75 | 731 |
| 7 | Aquaculture pond | 25 | 238 | 7 | Oil field | 72 | 612 |
| 8 | Paddy field | 87 | 745 | 8 | Sea | 116 | 756 |
| 9 | Estuarine area | 27 | 248 | 9 | Intertidal phragmite | 86 | 758 |
| 10 | River | 27 | 272 | 10 | Ecological reservoir | 75 | 563 |
| 11 | Woodland | 19 | 196 | 11 | Suaeda salsa | 67 | 610 |
| 12 | Barren | 25 | 129 | 12 | Salt fields | 81 | 663 |
| 13 | Building | 37 | 489 | 13 | Arable land | 68 | 681 |
| 14 | Fallow land | 26 | 208 | 14 | Phragmite | 83 | 756 |
| 15 | Rainfed cropland | 28 | 176 | 15 | Woodland | 49 | 502 |
| 16 | Suaeda salsa | 14 | 71 | 16 | Lotus pond | 75 | 461 |
| 17 | Irrigation canal | 10 | 28 | 17 | Typha orientalis presl | 6 | 30 |
| 18 | Phragmites | 12 | 120 | 18 | Robinia pseudoacacia | 65 | 516 |
| | | | | 19 | Pond | 86 | 763 |
| | | | | 20 | Yellow river | 88 | 771 |
| Total | | 744 | 7150 | Total | | 1462 | 12167 |

in Fig. 6 (c) and (d), the Yellow River Estuary dataset was collected by GF-5 satellite and Sentinel-2 satellite in the Yellow River Delta on November 1, 2018 and November 3, 2018, respectively. There are 285 bands in Yellow River Estuary HSI (the bad bands are 1 and 2 in VNIR and 42-53, 96-115, 119-121, 172-173, and 175-180 in SWIR), which spatial size is 1185×1342 pixels. The size of MSI is 3555×4026 pixels. It is located in the northeast of Shandong Province, China ($36^{\circ}55' - 38^{\circ}16'N$, $117^{\circ}31' - 119^{\circ}18'E$). The Yellow River estuary wetland is located in the east of the Yellow River Delta. Due to the great impact of salinization process in the current region, the vegetation mainly consists of holophytic plant communities dominated by grass and shrub species. The available label maps are manually annotated by experts with rich knowledge in field trips and photo interpretation. Table I lists training and testing samples randomly selected from ROI.

It is worth recalling that in Table I, mixed area 1 is the mixed area of phragmites and tamarix, mixed area 2 is the mixed tamarix and suaeda salsa, and mixed area 3 represents the mixed area of tamarix, phragmites and suaeda salsa. The ecological reservoir and phragmites are usually utilized for ecological restoration. Intertidal phragmites is distributed in intertidal zone with a small cover degree (less than 0.1). Low-tide mudflats and high-tide mudflats are located in intertidal zone, and differ in water content. In the Yellow River Delta, most of the robinia pseudoacacia are artificially cultivated, while woodland includes other alkali tolerant trees and shrubs. In addition, three widely used quantitative indicators: overall accuracy (OA), average accuracy (AA), and kappa coefficient (Kappa) are considered to evaluate classification performance.

B. Parameters Analysis of the Proposed Method

1) *Analysis of the Image Patch Size*: In this subsection, many important parameters are discussed. The first is the size of image patches. In this paper, r represents the square neighborhood information with radius $r/2 - 1$ around the central pixel. We set $r = [5, 7, 9, 11, 13, 15, 17]$, and a larger r means that more neighborhood information is involved. Fig. 8 indicates that when $r < 9$ the proposed method can hardly achieve excellent performance. When $r = 9$, the proposed DFINet achieves the highest OA value using the Yancheng dataset. A larger neighborhood area leads to worse results as the increase of r . For Yellow River Estuary dataset, the best result is realized at $r = 13$. Considering that when $r = 11$, the competitive result is obtained, and a larger value of r increases the computational burden. Therefore, we choose $r = 9$ and $r = 11$ for Yancheng dataset and Yellow River Estuary dataset, respectively.

2) *Analysis of the Hyperparameters*: In CNN, the loss function is the starting point of back propagation to update network weights. In this paper, the hyperparameters λ_1 and λ_2 control the contributions of the consistency loss and discrimination loss, respectively. Table II exhibits the relationship between OA and different hyperparameters of loss functions. As listed in Table II, $\lambda_1 = 0.1$ and $\lambda_2 = 0.01$ are chosen for optimization. For two datasets, $\lambda_2 = 0.5$ leads to gradient explosion. Although the higher OA values is obtained when $\lambda_2 = 0.1$, the training process fluctuates greatly. It is also vulnerable to gradient explosions. Generally speaking, DFINet achieves the promising results when $\lambda_2 = 0.01$. In addition, λ_1 has few effects on the performance. Therefore, to ensure

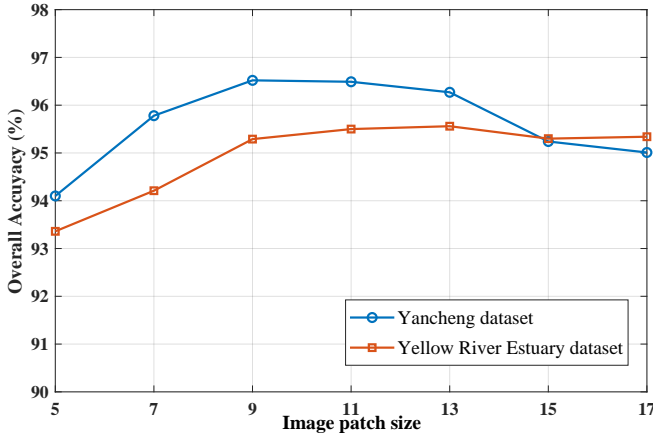


Fig. 8. Relationship between OA and the image patch size.

the generalization, $\lambda_1 = 0.1$ and $\lambda_2 = 0.01$ are the best choice for the proposed DFNet.

Besides, the consistency loss and discrimination loss are further separately analyzed. Table II lists that the discrimination loss achieves greater accuracy improvement. When only cross-entropy loss is optimized, the performance is worse, which also confirms the effectiveness of consistency loss and discrimination loss. Furthermore, the joint optimization of multiple loss functions is carried out to improve the classification accuracy.

TABLE II
RELATIONSHIP BETWEEN OA AND THE HYPERPARAMETERS OF LOSS FUNCTIONS.

| Yancheng dataset | $\lambda_2=0$ | $\lambda_2=0.01$ | $\lambda_2=0.1$ | $\lambda_2=0.5$ |
|------------------------------|---------------|------------------|-----------------|-----------------|
| $\lambda_1=0$ | 95.48 | 95.76 | 95.64 | — |
| $\lambda_1=0.01$ | 95.36 | 96.50 | 96.41 | — |
| $\lambda_1=0.1$ | 95.79 | 96.94 | 96.48 | — |
| $\lambda_1=0.5$ | 95.80 | 95.75 | 94.28 | — |
| $\lambda_1=1.0$ | 95.27 | 95.24 | 92.84 | — |
| Yellow River Estuary dataset | $\lambda_2=0$ | $\lambda_2=0.01$ | $\lambda_2=0.1$ | $\lambda_2=0.5$ |
| $\lambda_1=0$ | 93.71 | 95.09 | 93.02 | 87.35 |
| $\lambda_1=0.01$ | 92.68 | 95.34 | 92.87 | 92.02 |
| $\lambda_1=0.1$ | 93.65 | 95.61 | 95.19 | — |
| $\lambda_1=0.5$ | 93.32 | 95.42 | 93.94 | — |
| $\lambda_1=1.0$ | 91.70 | 92.03 | 92.55 | — |

3) *Analysis of the Learning Rate and the Number of Epochs*: In the training stage, an appropriate learning rate makes the objective function converge to the local minimum in a suitable time. We first set the learning rate Lr to 0.1, 0.01, 0.001, and 0.0001. Fig. 9 displays the relationship between training loss and the number of epochs.

From the curve, we can find that when the learning rate is 0.1, the training process has a huge fluctuation and the network is difficult to converge. When $Lr = 0.0001$, the proposed DFNet suffers from slow convergence. In contrast, when $Lr = 0.1$ and $Lr = 0.01$, the proposed DFNet tends to stabilize convergence. However, the training loss occasionally

unstable, when $Lr = 0.1$. Therefore, we choose $Lr = 0.1$ with step attenuation strategy, and use a weight decay of 0.0005 and momentum of 0.9. In addition, the number of epochs is set to 100.

4) *Analysis of Image Registration*: In this paper, only spatial registration of HSI and MSI is performed, and then feature fusion is executed instead of data fusion. The spatial resolutions of HSI and MSI are kept after registration, thus there is no loss of spatial information. In multi-scale PIIFD algorithm, Gaussian pyramid is constructed to reduce the mismatch of keypoints caused by scale difference.

The quality of registration is measured based on checkerboard form. To visually exhibit the registration effect, HSI is upsampled to the size of MSI, and then the local checkerboard forms of wetland datasets are shown in Fig. 10. Finally, the visual comparison is employed to ensure that the error between the sensed image (MSI) and reference image (HSI) is less than one pixel. For example, the texture consistency of landcover is achieved when HSI is used as a reference image. After that, the proposed DFNet is performed on HSI with ground truth map (30m spatial resolution) and the registered MSI (10m spatial resolution). In short, HSI and MSI achieve the consistent correspondence of spatial position, which is beneficial to the information integration.

C. Ablation Experiment

The ablation experiment is presented to verify the effectiveness of the designed DCAM. All experiments are implemented based on feature extraction network in Section II. Table III exhibits the relationship between different modules and OA/AA. In Table III, "Shared" means the weights are shared in feature extraction network. SE and CBAM represent the squeeze-and-excitation (SE) block in [41] and convolutional block attention module (CBAM) in [48]. Obviously, feature extraction network based on weight sharing is not conducive to information complementary. The full model with cross attention and depthwise correlation achieves the highest accuracy. There are 1.29% and 0.92% improvements in OA for the two experimental datasets compared with other versions. Cross attention is employed to learn the self-correlation of multi-source feature pairs. The cross-correlation is further achieved by depthwise correlation operator. From Table III, the OA is improved from 94.21% to 94.89% on Yellow River Estuary dataset with cross attention. Similarly, 0.24% improvement on Yancheng dataset with cross-correlation. In addition, other attention modules are introduced for comparison. It can be concluded that SE and CBAM learn important information from single source data. However, it is difficult to facilitate feature correlation without information interaction. Therefore, the improvements of OA are not significant. Specifically, at least 0.89% OA value and 1.82% AA value are increased on Yellow River Estuary dataset with DCAM. The AA values on Yancheng dataset are improved by at least 3.06%. Besides, though the improvements of OA are limit, the more satisfactory performance of few-shot classification is achieved by joint optimization. To sum up, the proposed DFNet benefits from DCAM which encourages the interaction of multisource feature pairs.

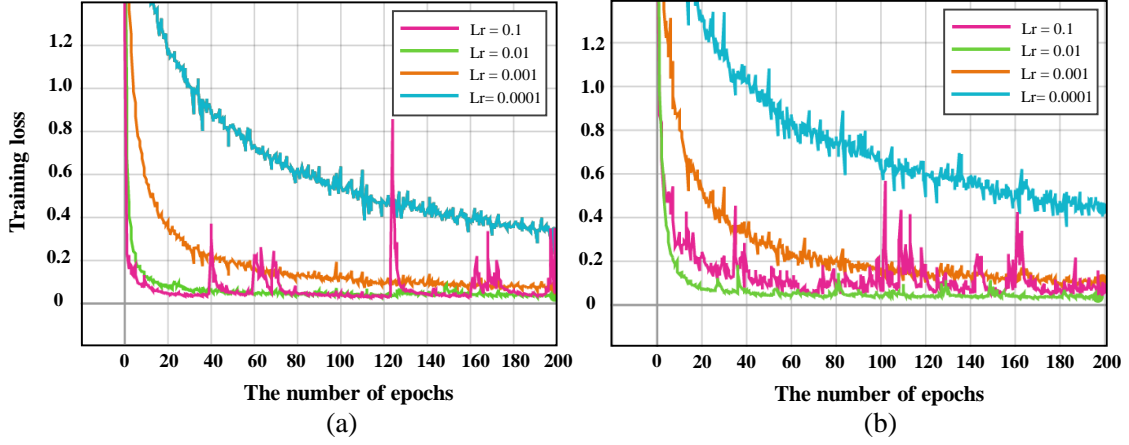


Fig. 9. Relationship among training loss, learning rate and the number of epochs. (a) Training loss on Yancheng dataset. (b) Training loss on Yellow River Estuary dataset.

TABLE III
ABLATION EXPERIMENT FOR THE PROPOSED DFINET ON TWO WETLAND DATASETS.

| Dataset | Shared | Cross attention | Depth correlation | Overall Accuracy / Average Accuracy (%) | |
|-----------|--------|-----------------|-------------------|---|------------------------------|
| | | | | Yancheng dataset | Yellow River Estuary dataset |
| Conv+DCAM | ✓ | ✓ | ✓ | 83.72 / 59.57 | 86.69 / 78.24 |
| Conv+DCAM | × | × | × | 96.04 / 88.98 | 94.21 / 93.87 |
| | | ✓ | × | 96.28 / 88.20 | 94.89 / 95.00 |
| | | × | ✓ | 96.11 / 87.91 | 94.30 / 93.98 |
| | | ✓ | ✓ | 96.94 / 92.17 | 95.61 / 96.37 |
| Conv+SE | × | — | — | 96.34 / 89.11 | 94.72 / 94.55 |
| Conv+CBAM | | | | 96.12 / 87.96 | 94.34 / 94.21 |

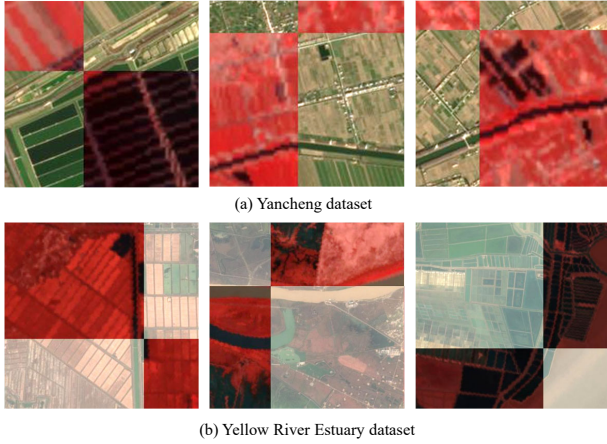


Fig. 10. The local checkerboard forms of wetland datasets. The scene under red mask comes from the HSI of GF-5, and the other is MSI of Sentinel-2.

D. Classification Performance

In order to verify the effectiveness of the proposed method, we compare DFINet with several related works, including SVM [49], LBP-ELM [50], Context CNN [51], Two-branch CNN [21]. SVM is implemented on the multisource data by the LIBSVM toolbox. In LBP-ELM, local binary pattern (LBP) is first utilized for feature representation, then the classification map is predicted by extreme learning machine

(ELM). Context CNN can optimally explore the interaction of context by using local space-spectral relations. In Two-branch CNN, the 1D/2D CNN and cascade block are elaborate designed for multisource data. HSI and MSI of wetland are used to verify the performance of DFINet. We express the HSI as GF-5, and the MSI as Sen-2. For instance, the GF-5 and Sen-2 mean the classification results obtained by HSI only and MSI only, respectively. And “GF-5 + Sen-2” denotes the classification for integration of HSI and MSI.

1) *Results on Yancheng Dataset:* In this subsection, the experiment is conducted to validate the performance of the proposed DFINet. In all the experiments, training and testing samples are selected as listed in Table I. For a visual evaluation of the performance, the full classification maps are provided in Fig. 11. In Fig. 11, SVM and LBP-ELM generate noisy maps, in which some aquaculture ponds are misclassified to pond or river by mistake. For the context CNN, the full classification map exhibits plenty of barren, which is inconsistent with the real distribution. It can be clearly noticed that the proposed DFINet produces a more accurate and noiseless full classification map, since multisource features have been fully interacted.

From Table IV, we observe that the methods mentioned above obtain high OA values on Yancheng dataset. Besides, the proposed method is still superior to other comparison methods on OA, AA, and Kappa. There is at least 1.37% OA improvement over other CNN-based methods. In particular, the

TABLE IV
CLASS-SPECIFIC CLASSIFICATION ACCURACY (%) USING DIFFERENT METHODS ON YANCHENG DATASET.

| No. | SVM | | | LBP-ELM | | | Context CNN | | | Two-branch CNN | | | DFINet |
|--------|---------------|--------|---------------|---------------|--------|---------------|---------------|--------|---------------|----------------|--------------|---------------|----------------------|
| | GF-5 | Sen-2 | GF-5+Sen2 | GF-5 | Sen-2 | GF-5+Sen2 | GF-5 | Sen-2 | GF-5+Sen2 | GF-5 | Sen-2 | GF-5+Sen2 | GF-5+Sen2 |
| 1 | 99.73 | 59.74 | 99.95 | 98.31 | 72.83 | 99.68 | 97.71 | 90.53 | 99.45 | 86.51 | 61.34 | 100.00 | 99.70±0.35 |
| 2 | 100.00 | 64.85 | 100.00 | 100.00 | 66.78 | 100.00 | 100.00 | 32.39 | 100.00 | 100.00 | 68.09 | 100.00 | 98.74±1.75 |
| 3 | 40.38 | 0.96 | 39.42 | 53.85 | 0.00 | 51.92 | 21.15 | 10.58 | 32.69 | 36.54 | 51.92 | 5.77 | 58.85±6.60 |
| 4 | 77.46 | 53.76 | 75.72 | 83.24 | 59.54 | 73.99 | 81.50 | 57.80 | 69.94 | 91.33 | 61.27 | 83.24 | 78.38±5.60 |
| 5 | 98.68 | 57.89 | 100.00 | 100.00 | 73.68 | 100.00 | 34.21 | 40.79 | 53.95 | 96.05 | 89.47 | 100.00 | 100.00±0.00 |
| 6 | 81.07 | 95.06 | 88.48 | 88.07 | 93.42 | 90.12 | 95.06 | 94.24 | 87.65 | 89.71 | 93.42 | 88.48 | 95.51±0.81 |
| 7 | 83.19 | 66.81 | 72.69 | 90.34 | 62.61 | 71.43 | 92.44 | 73.11 | 96.64 | 94.96 | 83.61 | 100.00 | 88.87±2.36 |
| 8 | 98.12 | 80.81 | 99.33 | 97.99 | 81.34 | 98.52 | 100.00 | 80.13 | 98.52 | 99.73 | 80.67 | 98.79 | 98.95±0.57 |
| 9 | 99.19 | 87.90 | 98.39 | 97.58 | 68.15 | 98.79 | 94.35 | 95.97 | 100.00 | 99.60 | 97.18 | 100.00 | 99.84±0.51 |
| 10 | 81.62 | 91.91 | 83.82 | 87.87 | 86.76 | 88.97 | 98.53 | 98.16 | 98.53 | 95.59 | 94.85 | 97.79 | 98.64±0.63 |
| 11 | 100.00 | 83.16 | 100.00 | 100.00 | 74.49 | 100.00 | 100.00 | 89.29 | 100.00 | 100.00 | 90.82 | 100.00 | 100.00±0.00 |
| 12 | 100.00 | 97.67 | 100.00 | 100.00 | 92.25 | 100.00 | 86.82 | 34.88 | 94.57 | 98.45 | 99.22 | 98.45 | 99.46±0.82 |
| 13 | 80.78 | 91.21 | 84.46 | 66.87 | 86.91 | 72.60 | 93.66 | 96.11 | 93.25 | 97.75 | 99.80 | 88.14 | 99.37±0.57 |
| 14 | 91.83 | 26.92 | 99.52 | 99.04 | 41.83 | 99.04 | 91.83 | 78.85 | 95.19 | 99.04 | 9.62 | 92.31 | 94.86±4.03 |
| 15 | 89.20 | 74.43 | 97.73 | 89.77 | 64.77 | 96.02 | 82.39 | 32.39 | 81.82 | 80.11 | 82.95 | 93.75 | 95.91±2.62 |
| 16 | 83.10 | 60.56 | 71.83 | 88.73 | 73.24 | 84.51 | 61.97 | 32.39 | 76.06 | 64.79 | 91.55 | 80.28 | 70.14±4.82 |
| 17 | 75.00 | 57.14 | 82.14 | 75.00 | 75.00 | 78.57 | 100.00 | 82.14 | 100.00 | 92.86 | 57.14 | 100.00 | 100.00±0.00 |
| 18 | 54.17 | 51.67 | 58.33 | 60.00 | 53.33 | 71.67 | 48.33 | 79.17 | 86.67 | 71.67 | 58.33 | 70.83 | 81.92±8.44 |
| OA (%) | 93.51 | 68.34 | 94.29 | 93.50 | 71.79 | 93.96 | 93.75 | 71.99 | 95.29 | 92.42 | 72.62 | 95.72 | 96.94±0.23 |
| AA (%) | 85.20 | 66.80 | 86.21 | 87.59 | 68.16 | 87.55 | 0.82 | 66.61 | 86.94 | 88.59 | 76.18 | 88.77 | 92.17±0.66 |
| Kappa | 0.9228 | 0.6267 | 0.9321 | 0.9229 | 0.6651 | 0.9282 | 0.9258 | 0.6630 | 0.9440 | 0.9110 | 0.6778 | 0.9491 | 0.9636±0.0035 |

proposed method outperforms other methods in some regions with fewer training samples (class-3, class-17, and class-18). It should be noted that it is difficult to achieve promising results when only MSI is used for classification, which suggests MSI cannot fully support more detailed classification. When HSI is introduced, abundant spectral information provides more comprehensive information for interpretation. In the context CNN, the accuracy of class-12 is improved from 65.15% to 78.23%. In the two-branch CNN, the accuracy of class-15 is increased by 13.64% with the integration of MSI. The proposed DFNet shows a relatively stable performance by integrating the advantages of HSI and MSI compared with other competitors. However, the accuracies of class 3 and class 16 are much lower than the AA in Table IV. Especially in class 3, salt field is wrongly divided into barren, and some pixels of suaeda salsa are misclassified to mudflat. As we know, the vegetation coverage in salt field without seawater pouring is very low, thus resulting in lower discrimination between salt field and barren. Similarly, suaeda salsa is unreasonably divided into mudflat due to the lower coverage.

2) *Results on Yellow River Estuary Dataset:* The classification maps of entire image scenes are presented in Fig. 12. In Fig. 12 (b) and (d), many pixels belonging to sea are misclassified to ecological reservoirs. A larger amount of noise deteriorates the classification maps quality of SVM and LBP-ELM. The CNN-based methods generate clearer full classification maps. For the context CNN, some unreasonable distribution in the produced map degrades the performance of classification. For example, sea pixels appears in the land area, and the salt field and ecological reservoir exhibit unreasonable mixture. In addition, there are a lot of noise regions in the sea. In Fig. 12 (d), the mixed area 2 mixing tamarix and suaeda salsa is wrongly divided, because suaeda salsa usually grows in saline and alkaline land. In contrast, DFNet produces a

more accurate full classification map which is closer to the real distribution.

Table V provides quantitative assessment. It can be observed that DFNet consistently outperforms other methods. Compared with the traditional machine learning methods, SVM and LBP-ELM have weak classification performance. Because the information of HSI and MSI is complex, it is difficult to map complex feature representation through a shallow model. In particular, though the fusion of multisource information adds complementary information, more redundant information is introduced. This also aggravates the phenomenon of “dimensional disaster”, which leads to the reduction of OA. The performance of deep learning method is significantly improved compared with traditional machine learning methods. Obviously, the results are improved by feature fusion. The DFNet obtains the best classification results on Yellow River Estuary dataset. Moreover, the proposed method achieves remarkable accuracy improvement in the mixed areas (classes 4-6) in which the performance of most comparison methods fluctuates greatly. Besides, Table V lists that the proposed DFNet accurately distinguishes the land-cover of Yellow River Estuary wetland, such as classes (1-4) and classes (17-20). However, there are still two typical classes (i.e., class 12 and class 16) that are difficult to be separated. For class 12, the salt field is misjudged to pond. We speculate that the water in salt field misleads feature extraction. In addition, class 16 represents lotus pond which is misclassified as arable land. To our best knowledge, in November, the Yellow River Estuary wetland is in winter, and the lotus pond entered the dry season with vegetation withering. Therefore, some regions exhibit similar characteristics with arable land, leading to misjudgment. In general, the proposed DFNet precisely reflects the spatial and spectral features of land-cover in Yellow River Estuary wetland.

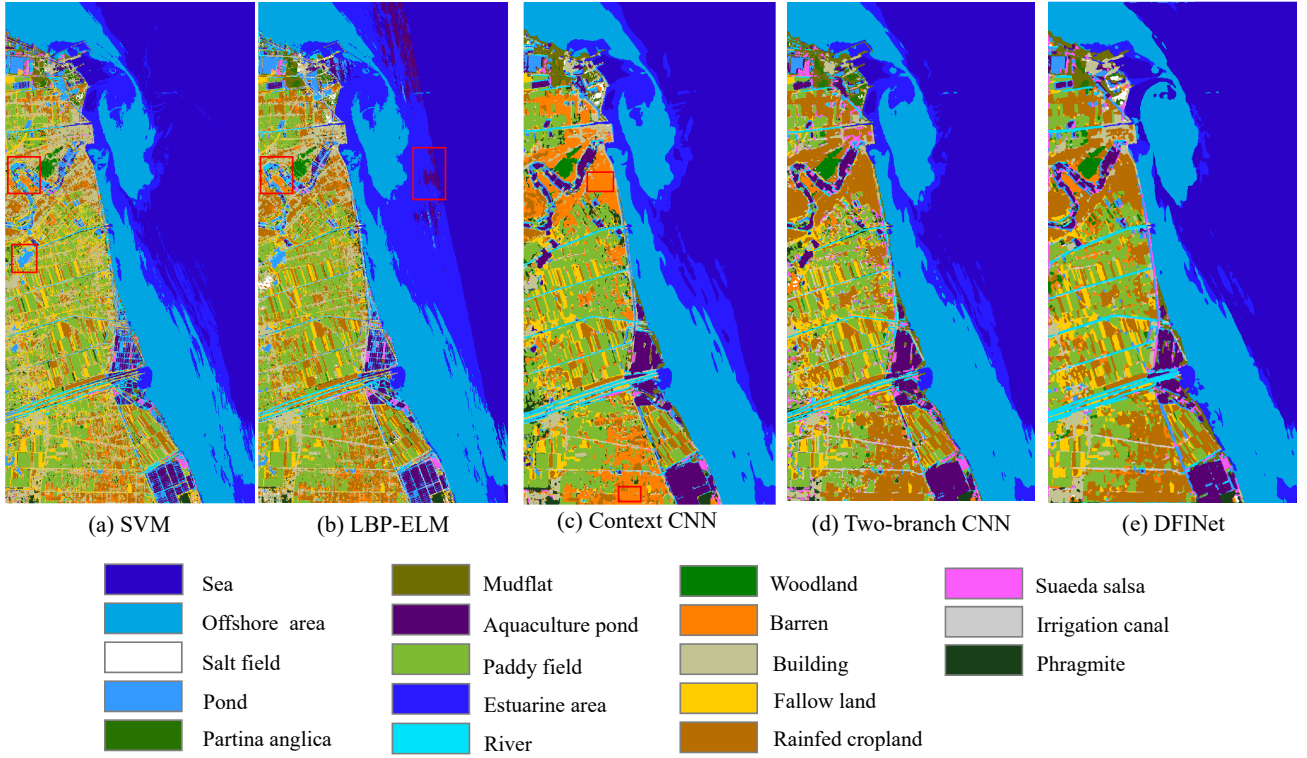


Fig. 11. Full classification maps using different methods on Yancheng dataset.

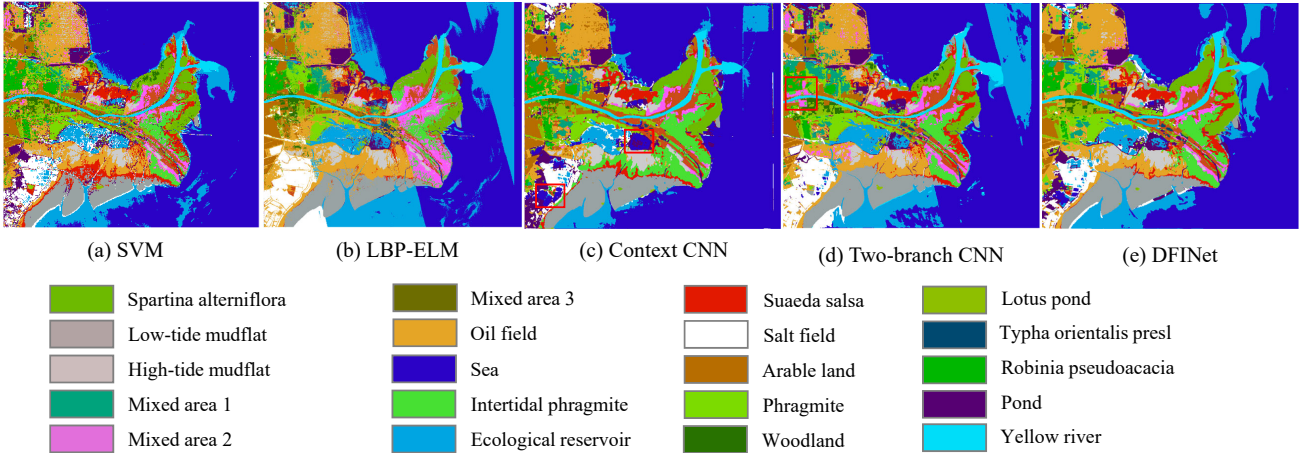


Fig. 12. Full classification maps using different methods on Yellow River Estuary dataset.

To sum up, the cooperation of HSI and MSI improves the performance of wetland classification, which confirms the complementary merits of multisource information and the effect of image registration. Comparative experiments show the superior performance of the proposed DFINet in most classes. Aiming at several typical classes with low class accuracy, the deeply interpretation of multisource wetland data will be carried out in future works by combining the interspecific relationship and distribution attributes.

3) *Analysis of Number of Training Samples*: Labeled samples are very crucial in machine learning. However, data labeling is time-consuming and laborious in remote sensing

data. Thus, a small amount of labeled data is available to process remote sensing data. Consider the fact that few training samples are sensitive to over-fitting. In this subsection, we explore the relationship between the number of training samples and OA on two wetland datasets.

Here, we randomly select [20%, 40%, 60%, 80%] samples from training set. The experiments are conducted 10 times, then the average results are reported. As shown in Fig. 13 and Fig. 14, the OA values tend to decrease as the number of training samples decreases. From the curves, there is a sharp increase from 20% to 60%. Especially, significant effect deterioration occurs in the result of Context CNN. This is

TABLE V
CLASS-SPECIFIC CLASSIFICATION ACCURACY (%) USING DIFFERENT METHODS ON YELLOW RIVER ESTUARY DATASET.

| No. | SVM | | | LBP-ELM | | | Context CNN | | | Two-branch CNN | | | DFINet |
|--------|---------------|---------------|---------------|---------------|---------------|---------------|---------------|---------------|---------------|----------------|---------------|---------------|----------------------|
| | GF-5 | Sen-2 | GF-5+Sen-2 | GF-5 | Sen-2 | GF-5+Sen-2 | GF-5 | Sen-2 | GF-5+Sen-2 | GF-5 | Sen-2 | GF-5+Sen-2 | GF-5+Sen-2 |
| 1 | 99.87 | 56.66 | 65.14 | 47.51 | 66.76 | 47.64 | 100.00 | 83.04 | 100.00 | 67.83 | 81.43 | 100.00 | 100.00±0.00 |
| 2 | 100.00 | 90.97 | 100.00 | 100.00 | 90.69 | 100.00 | 100.00 | 98.87 | 100.00 | 100.00 | 100.00 | 93.37 | 100.00±0.00 |
| 3 | 94.11 | 100.00 | 94.11 | 94.26 | 100.00 | 94.42 | 100.00 | 100.00 | 99.53 | 98.76 | 98.60 | 100.00 | 100.00±0.00 |
| 4 | 95.93 | 84.55 | 98.37 | 92.68 | 94.31 | 95.93 | 100.00 | 97.56 | 100.00 | 100.00 | 100.00 | 100.00 | 100.00±0.00 |
| 5 | 35.40 | 93.67 | 48.06 | 45.35 | 94.57 | 73.64 | 76.61 | 86.43 | 67.44 | 53.62 | 74.16 | 86.30 | 95.41±6.41 |
| 6 | 81.67 | 83.72 | 81.26 | 79.21 | 83.72 | 80.30 | 87.00 | 99.18 | 84.95 | 95.21 | 90.70 | 85.36 | 94.12±3.11 |
| 7 | 73.20 | 70.92 | 72.06 | 77.94 | 59.15 | 74.02 | 65.69 | 64.54 | 95.59 | 97.88 | 96.90 | 96.24 | 99.85±0.29 |
| 8 | 100.00 | 100.00 | 100.00 | 100.00 | 100.00 | 100.00 | 100.00 | 100.00 | 100.00 | 100.00 | 100.00 | 100.00 | 100.00±0.00 |
| 9 | 95.51 | 97.10 | 96.17 | 95.78 | 96.97 | 95.78 | 100.00 | 100.00 | 100.00 | 100.00 | 100.00 | 100.00 | 96.98±0.08 |
| 10 | 87.39 | 84.01 | 87.57 | 92.90 | 88.28 | 92.01 | 100.00 | 96.09 | 100.00 | 100.00 | 100.00 | 97.87 | 99.41±0.86 |
| 11 | 91.15 | 100.00 | 93.44 | 42.46 | 99.84 | 45.41 | 84.10 | 100.00 | 90.98 | 82.46 | 98.20 | 100.00 | 95.90±5.38 |
| 12 | 73.60 | 61.99 | 73.91 | 64.86 | 73.30 | 68.02 | 80.54 | 66.97 | 80.39 | 62.75 | 62.75 | 68.63 | 66.53±4.12 |
| 13 | 99.85 | 99.71 | 99.85 | 100.00 | 99.56 | 100.00 | 97.80 | 100.00 | 100.00 | 100.00 | 100.00 | 99.71 | 100.00±0.00 |
| 14 | 80.56 | 71.69 | 78.97 | 90.87 | 91.14 | 90.87 | 98.54 | 98.54 | 100.00 | 100.00 | 100.00 | 89.29 | 100.00±0.00 |
| 15 | 83.67 | 91.83 | 91.43 | 92.63 | 98.21 | 96.81 | 92.23 | 98.80 | 85.66 | 99.20 | 100.00 | 98.80 | 95.27±3.21 |
| 16 | 38.18 | 38.39 | 38.39 | 42.52 | 39.26 | 41.87 | 51.19 | 46.20 | 60.09 | 42.08 | 41.00 | 63.12 | 60.86±14.56 |
| 17 | 100.00 | 100.00 | 100.00 | 100.00 | 100.00 | 100.00 | 100.00 | 100.00 | 100.00 | 100.00 | 100.00 | 100.00 | 100.00±0.00 |
| 18 | 95.35 | 98.06 | 99.22 | 89.34 | 93.02 | 98.26 | 98.06 | 98.06 | 99.81 | 100.00 | 99.61 | 100.00 | 100.00±0.00 |
| 19 | 93.45 | 98.43 | 93.32 | 98.43 | 96.85 | 98.03 | 97.77 | 94.23 | 97.77 | 100.00 | 100.00 | 96.85 | 100.00±0.00 |
| 20 | 100.00 | 100.00 | 100.00 | 100.00 | 100.00 | 100.00 | 100.00 | 100.00 | 100.00 | 100.00 | 100.00 | 100.00 | 100.00±0.00 |
| OA (%) | 85.49 | 86.21 | 84.69 | 81.59 | 88.35 | 84.09 | 91.54 | 92.23 | 93.00 | 89.49 | 92.06 | 93.54 | 95.61±0.37 |
| AA (%) | 85.94 | 86.09 | 85.56 | 82.34 | 88.28 | 84.65 | 91.48 | 91.43 | 93.11 | 89.99 | 92.17 | 93.78 | 96.37±0.49 |
| Kappa | 0.8464 | 0.8540 | 0.8380 | 0.8052 | 0.8767 | 0.8316 | 0.9104 | 0.9108 | 0.9260 | 0.8888 | 0.9160 | 0.9316 | 0.9535±0.0039 |

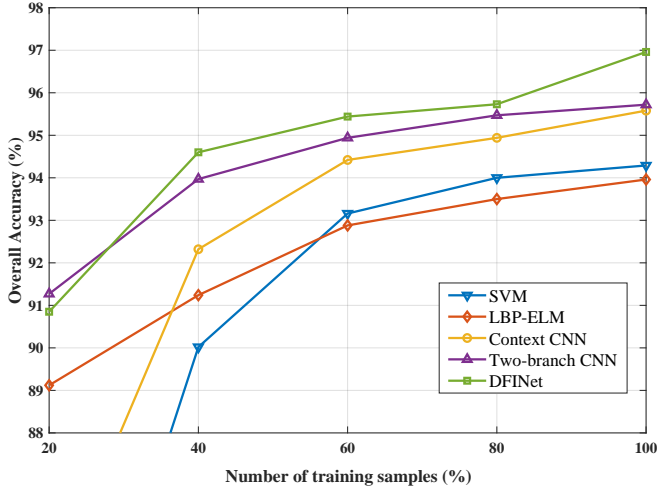


Fig. 13. Relationship between OA and the number of training samples on Yancheng dataset.

because fewer training samples lead to over-fitting. In contrast, other CNN-based competitors alleviate the over-fitting through some strategies. For example, the two-branch CNN increases the number of training samples through data augmentation. Although data augmentation is effective, a large amount of computational cost is introduced. In this paper, DFNet standardizes the training process by using multiple loss functions. In other words, the biased estimation generates the solution in a smaller range, so it achieves satisfactory performance of few-shot classification.

4) *Running Time on Two Wetland Dataset:* The running time of the proposed DFNet and other comparison methods is reported in Table VI. All experiments are implemented

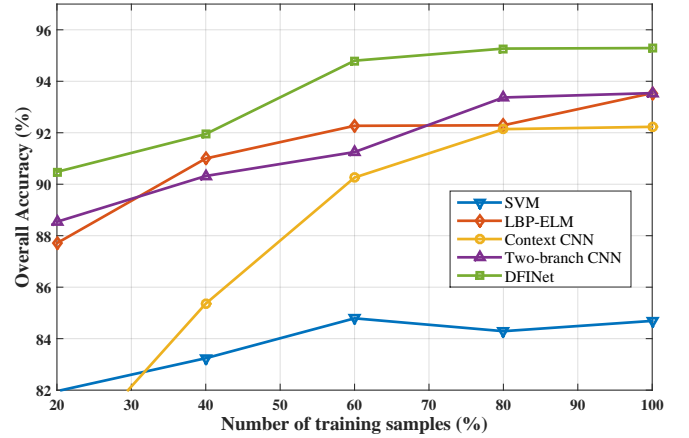


Fig. 14. Relationship between OA and the number of training samples on Yellow River Estuary dataset.

on CPU (Intel Core i7-9700@3.00GHz) with Matlab2019b, while CNN-based methods make extra use of the GPU (Nvidia GTX 1060) platform. From Table VI, SVM and LBP-ELM reach higher computing efficiency. In particular, the LBP-ELM completes the classification within 5 seconds, which is because the low dimension of LBP features. Context CNN develops a deeper and wider structure, thus it is necessary to optimize more parameters which are time-consuming. In two-branch CNN, data augmentation and multi-stage learning spend much time. The running time is increased exponentially with increases of data. The proposed DFNet is more efficient than other CNN-based methods. Considering running time and OA, DFNet serves as a good candidate for wetland classification.

TABLE VI
RUNNING TIME (IN SECONDS) ON TWO WETLAND DATASETS.

| Dataset | Yancheng dataset | | Yellow River Estuary dataset | |
|----------------|------------------|--------|------------------------------|--------|
| Method | Running time (s) | OA (%) | Running time (s) | OA (%) |
| SVM | 17.71 | 94.29 | 39.02 | 84.69 |
| LBP-ELM | 2.61 | 93.96 | 4.77 | 84.09 |
| Context CNN | 174.11 | 95.58 | 294.66 | 92.23 |
| Two-branch CNN | 380.25 | 95.72 | 972.38 | 93.54 |
| DFINet | 72.21 | 96.94 | 98.60 | 95.61 |

IV. CONCLUSION

In this paper, a novel deep-feature model has been proposed for coastal wetland classification using multisource satellite remote sensing data. The benefits of the proposed DFINet mainly come from two aspects. On the one hand, the depthwise cross attention module is designed to utilize the complementary merits from HSI and MSI. The attention mechanism based on local feature pair correlation is firstly deployed to emphasize the meaningful spatial information. After that, the correlation of global feature pairs promotes feature integration. On the other hand, we encourage the consistency of HSI and MSI by minimizing the consistency loss, and the feature discrimination is regularized by discrimination loss. Extensive experiments, on two wetland datasets of Yellow River Estuary and Yancheng, reveal the effectiveness of the proposed DFINet compared with other state-of-the-art classification techniques.

REFERENCES

- [1] A. Aslan, A. F. Rahman, M. W. Warren, and S. M. Robeson, "Mapping spatial distribution and biomass of coastal wetland vegetation in Indonesian papua by combining active and passive remotely sensed data," *Remote Sensing of Environment*, vol. 183, pp. 65–81, 2016.
- [2] M. Schuerch, T. Spencer, S. Temmerman, M. L. Kirwan, C. Wolff, D. Lincke, C. J. McOwen, M. D. Pickering, R. Reef, A. T. Vafeidis *et al.*, "Future response of global coastal wetlands to sea-level rise," *Nature*, vol. 561, no. 7722, pp. 231–234, 2018.
- [3] S. Mahdavi, B. Salehi, J. Granger, M. Amani, B. Brisco, and W. Huang, "Remote sensing for wetland classification: A comprehensive review," *GIScience & Remote Sensing*, vol. 55, no. 5, pp. 623–658, 2018.
- [4] C. Munyati, "Wetland change detection on the kafue flats, zambia, by classification of a multitemporal remote sensing image dataset," *International journal of remote sensing*, vol. 21, no. 9, pp. 1787–1806, 2000.
- [5] R. J. Zomer, A. Trabucco, and S. Ustin, "Building spectral libraries for wetlands land cover classification and hyperspectral remote sensing," *Journal of environmental management*, vol. 90, no. 7, pp. 2170–2177, 2009.
- [6] A. Hirano, M. Madden, and R. Welch, "Hyperspectral image data for mapping wetland vegetation," *Wetlands*, vol. 23, no. 2, pp. 436–448, 2003.
- [7] M. Rezaee, M. Mahdianpari, Y. Zhang, and B. Salehi, "Deep convolutional neural network for complex wetland classification using optical remote sensing imagery," *IEEE Journal of Selected Topics in Applied Earth Observations and Remote Sensing*, vol. 11, no. 9, pp. 3030–3039, 2018.
- [8] M. Mahdianpari, B. Salehi, F. Mohammadimanesh, B. Brisco, S. Mahdavi, M. Amani, and J. E. Granger, "Fisher linear discriminant analysis of coherency matrix for wetland classification using polar imagery," *Remote Sensing of Environment*, vol. 206, pp. 300–317, 2018.
- [9] E. R. DeLancey, J. F. Simms, M. Mahdianpari, B. Brisco, C. Mahoney, and J. Kariyeva, "Comparing deep learning and shallow learning for large-scale wetland classification in alberta, canada," *Remote Sensing*, vol. 12, no. 1, p. 2, 2020.
- [10] H. Pan, "A feature sequence-based 3d convolutional method for wetland classification from multispectral images," *Remote Sensing Letters*, vol. 11, no. 9, pp. 837–846, 2020.
- [11] H. Su, W. Yao, Z. Wu, P. Zheng, and Q. Du, "Kernel low-rank representation with elastic net for china coastal wetland land cover classification using gf-5 hyperspectral imagery," *ISPRS Journal of Photogrammetry and Remote Sensing*, vol. 171, pp. 238–252, 2021.
- [12] C. Liu, R. Tao, W. Li, M. Zhang, W. Sun, and Q. Du, "Joint classification of hyperspectral and multispectral images for mapping coastal wetlands," *IEEE Journal of Selected Topics in Applied Earth Observations and Remote Sensing*, vol. 14, pp. 982–996, 2021.
- [13] M. Mahdianpari, B. Salehi, F. Mohammadimanesh, and M. Motagh, "Random forest wetland classification using alos-2 l-band, radarsat-2 c-band, and terrasars-x imagery," *ISPRS Journal of Photogrammetry and Remote Sensing*, vol. 130, pp. 13–31, 2017.
- [14] Y. Hu, J. Zhang, Y. Ma, J. An, G. Ren, and X. Li, "Hyperspectral coastal wetland classification based on a multiobject convolutional neural network model and decision fusion," *IEEE Geoscience and Remote Sensing Letters*, vol. 16, no. 7, pp. 1110–1114, 2019.
- [15] X. Han, J. Pan, and A. Devlin, "Remote sensing study of wetlands in the pearl river delta during 1995–2015 with the support vector machine method," *Frontiers of Earth Science*, vol. 12, 10 2017.
- [16] J. Hu, D. Hong, and X. X. Zhu, "Mima: Mapper-induced manifold alignment for semi-supervised fusion of optical image and polarimetric sar data," *IEEE Transactions on Geoscience and Remote Sensing*, vol. 57, no. 11, pp. 9025–9040, 2019.
- [17] M. Khodadadzadeh, J. Li, S. Prasad, and A. Plaza, "Fusion of hyperspectral and lidar remote sensing data using multiple feature learning," *IEEE Journal of Selected Topics in Applied Earth Observations and Remote Sensing*, vol. 8, no. 6, pp. 2971–2983, 2015.
- [18] J. Yang, G. Ren, Y. Ma, and Y. Fan, "Coastal wetland classification based on high resolution sar and optical image fusion," in *2016 IEEE International Geoscience and Remote Sensing Symposium (IGARSS)*, 2016, pp. 886–889.
- [19] Y. Zhang and S. Prasad, "Multisource geospatial data fusion via local joint sparse representation," *IEEE Transactions on Geoscience and Remote Sensing*, vol. 54, no. 6, pp. 3265–3276, 2016.
- [20] Y. Chen, C. Li, P. Ghamisi, X. Jia, and Y. Gu, "Deep fusion of remote sensing data for accurate classification," *IEEE Geoscience and Remote Sensing Letters*, vol. 14, no. 8, pp. 1253–1257, 2017.
- [21] X. Xu, W. Li, Q. Ran, Q. Du, L. Gao, and B. Zhang, "Multisource remote sensing data classification based on convolutional neural network," *IEEE Transactions on Geoscience and Remote Sensing*, vol. 56, no. 2, pp. 937–949, 2018.
- [22] M. Zhang, W. Li, Q. Du, L. Gao, and B. Zhang, "Feature extraction for classification of hyperspectral and lidar data using patch-to-patch cnn," *IEEE Transactions on Cybernetics*, vol. 50, no. 1, pp. 100–111, 2020.
- [23] P. Ghamisi, B. Höfle, and X. X. Zhu, "Hyperspectral and lidar data fusion using extinction profiles and deep convolutional neural network," *IEEE Journal of Selected Topics in Applied Earth Observations and Remote Sensing*, vol. 10, no. 6, pp. 3011–3024, 2017.
- [24] H. Li, P. Ghamisi, U. Soergel, and X. Zhu, "Hyperspectral and lidar fusion using deep three-stream convolutional neural networks," *Remote Sensing*, vol. 10, no. 10, p. 1649, 2018.
- [25] X. Zhao, R. Tao, W. Li, H. C. Li, Q. Du, W. Liao, and W. Philips, "Joint classification of hyperspectral and lidar data using hierarchical random walk and deep cnn architecture," *IEEE Transactions on Geoscience and Remote Sensing*, vol. 58, no. 10, pp. 7355–7370, 2020.
- [26] Y. Gu and Q. Wang, "Discriminative graph-based fusion of hsi and lidar data for urban area classification," *IEEE Geoscience and Remote Sensing Letters*, vol. 14, no. 6, pp. 906–910, 2017.
- [27] W. Liao, A. Pižurica, R. Bellens, S. Gautama, and W. Philips, "Generalized graph-based fusion of hyperspectral and lidar data using morphological features," *IEEE Geoscience and Remote Sensing Letters*, vol. 12, no. 3, pp. 552–556, 2015.
- [28] Y. Zhang, H. L. Yang, S. Prasad, E. Pasolli, J. Jung, and M. Crawford, "Ensemble multiple kernel active learning for classification of multi-source remote sensing data," *IEEE Journal of Selected Topics in Applied Earth Observations and Remote Sensing*, vol. 8, no. 2, pp. 845–858, 2015.
- [29] Y. Zhong, Q. Cao, J. Zhao, A. Ma, B. Zhao, and L. Zhang, "Optimal decision fusion for urban land-use/land-cover classification based on adaptive differential evolution using hyperspectral and lidar data," *Remote Sensing*, vol. 9, p. 868, 08 2017.
- [30] R. Hang, Z. Li, P. Ghamisi, D. Hong, G. Xia, and Q. Liu, "Classification of hyperspectral and lidar data using coupled cnns," *IEEE Transactions on Geoscience and Remote Sensing*, vol. 58, no. 7, pp. 4939–4950, 2020.
- [31] W. Liao, R. Bellens, A. Pižurica, S. Gautama, and W. Philips, "Combining feature fusion and decision fusion for classification of hyperspectral

- and lidar data,” in *2014 IEEE Geoscience and Remote Sensing Symposium*, 2014, pp. 1241–1244.
- [32] H. Li, Y. Ma, K. Liang, and Y. Yu, “Rapid matching algorithm for hyperspectral image based on norm sifting,” *Chinese Optics Letters*, vol. 10, no. 1, p. 013001, 2012.
 - [33] F. Fan, Y. Ma, C. Li, X. Mei, J. Huang, and J. Ma, “Hyperspectral image denoising with superpixel segmentation and low-rank representation,” *Information Sciences*, vol. 397, pp. 48–68, 2017.
 - [34] D. Hong, N. Yokoya, J. Chanussot, and X. X. Zhu, “Cospace: Common subspace learning from hyperspectral-multispectral correspondences,” *IEEE Transactions on Geoscience and Remote Sensing*, vol. 57, no. 7, pp. 4349–4359, 2019.
 - [35] C. Gao and W. Li, “Multi-scale piifd for registration of multi-source remote sensing images,” 2021.
 - [36] J. Chen, J. Tian, N. Lee, J. Zheng, R. T. Smith, and A. F. Laine, “A partial intensity invariant feature descriptor for multimodal retinal image registration,” *IEEE Transactions on Biomedical Engineering*, vol. 57, no. 7, pp. 1707–1718, 2010.
 - [37] J. S. Beis and D. G. Lowe, “Shape indexing using approximate nearest-neighbour search in high-dimensional spaces,” in *Conference on Computer Vision Pattern Recognition*, 1997.
 - [38] K. Xu, M. Qin, F. Sun, Y. Wang, Y.-K. Chen, and F. Ren, “Learning in the frequency domain,” in *Proceedings of the IEEE/CVF Conference on Computer Vision and Pattern Recognition*, 2020, pp. 1740–1749.
 - [39] T. Baltrušaitis, C. Ahuja, and L. Morency, “Multimodal machine learning: A survey and taxonomy,” *IEEE Transactions on Pattern Analysis and Machine Intelligence*, vol. 41, no. 2, pp. 423–443, 2019.
 - [40] J. Zeng, Y. Tong, Y. Huang, Q. Yan, W. Sun, J. Chen, and Y. Wang, “Deep surface normal estimation with hierarchical rgb-d fusion,” in *Proceedings of the IEEE Conference on Computer Vision and Pattern Recognition*, 2019, pp. 6153–6162.
 - [41] J. Hu, L. Shen, and G. Sun, “Squeeze-and-excitation networks,” in *2018 IEEE/CVF Conference on Computer Vision and Pattern Recognition*, 2018, pp. 7132–7141.
 - [42] X. Mei, E. Pan, Y. Ma, X. Dai, J. Huang, F. Fan, Q. Du, H. Zheng, and J. Ma, “Spectral-spatial attention networks for hyperspectral image classification,” *Remote Sensing*, vol. 11, no. 8, p. 963, 2019.
 - [43] M. Liu and H. Yin, “Cross attention network for semantic segmentation,” in *2019 IEEE International Conference on Image Processing (ICIP)*, 2019, pp. 2434–2438.
 - [44] S. Mohla, S. Pande, B. Banerjee, and S. Chaudhuri, “Fusatnet: Dual attention based spectrospatial multimodal fusion network for hyperspectral and lidar classification,” in *2020 IEEE/CVF Conference on Computer Vision and Pattern Recognition Workshops (CVPRW)*, 2020, pp. 416–425.
 - [45] Y. Wang, W. Huang, F. Sun, T. Xu, Y. Rong, and J. Huang, “Deep multimodal fusion by channel exchanging,” *Advances in Neural Information Processing Systems*, vol. 33, 2020.
 - [46] L. Zhen, P. Hu, X. Wang, and D. Peng, “Deep supervised cross-modal retrieval,” in *2019 IEEE/CVF Conference on Computer Vision and Pattern Recognition (CVPR)*, 2019, pp. 10 386–10 395.
 - [47] L. Jiao, W. Sun, G. Yang, G. Ren, and Y. Liu, “A hierarchical classification framework of satellite multispectral/hyperspectral images for mapping coastal wetlands,” *Remote Sensing*, vol. 11, no. 19, p. 2238, 2019.
 - [48] S. Woo, J. Park, J.-Y. Lee, and I. So Kweon, “Cbam: Convolutional block attention module,” in *Proceedings of the European conference on computer vision (ECCV)*, 2018, pp. 3–19.
 - [49] F. Melgani and L. Bruzzone, “Classification of hyperspectral remote sensing images with support vector machines,” *IEEE Transactions on Geoscience and Remote Sensing*, vol. 42, no. 8, pp. 1778–1790, 2004.
 - [50] W. Li, C. Chen, H. Su, and Q. Du, “Local binary patterns and extreme learning machine for hyperspectral imagery classification,” *IEEE Transactions on Geoscience and Remote Sensing*, vol. 53, no. 7, pp. 3681–3693, 2015.
 - [51] H. Lee and H. Kwon, “Going deeper with contextual cnn for hyperspectral image classification,” *IEEE Transactions on Image Processing*, vol. 26, no. 10, pp. 4843–4855, 2017.